Title

Atomically thin three-dimensional membranes of van der Waals semiconductors by wafer-scale growth.

Journal

Science Advances, 5(7)

Authors

Jin, Gangtae

Lee, Chang-Soo

Liao, Xing

et al.

Publication Date

2019-07-01

DOI

10.1126/sciadv.aaw3180

Peer reviewed

MATERIALS SCIENCE

Atomically thin three-dimensional membranes of van der Waals semiconductors by wafer-scale growth

Gangtae Jin[1,2]*, Chang-Soo Lee[1,2]*, Xing Liao[3], Juho Kim[1,2], Zhen Wang[4], Odongo Francis Ngome Okello[2], Bumsu Park[4], Jaehyun Park[1,2], Cheolhee Han[1,2], Hoseok Heo[3], Jonghwan Kim[2], Sang Ho Oh[4], Si-Young Choi[2], Hongkun Park[3], Moon-Ho Jo[1,2]†

We report wafer-scale growth of atomically thin, three-dimensional (3D) van der Waals (vdW) semiconductor membranes. By controlling the growth kinetics in the near-equilibrium limit during metal-organic chemical vapor depositions of MoS_2 and WS_2 monolayer (ML) crystals, we have achieved conformal ML coverage on diverse 3D texture substrates, such as periodic arrays of nanoscale needles and trenches on quartz and SiO_2/Si substrates. The ML semiconductor properties, such as channel resistivity and photoluminescence, are verified to be seamlessly uniform over the 3D textures and are scalable to wafer scale. In addition, we demonstrated that these 3D films can be easily delaminated from the growth substrates to form suspended 3D semiconductor membranes. Our work suggests that vdW ML semiconductor films can be useful platforms for patchable membrane electronics with atomic precision, yet large areas, on arbitrary substrates.

INTRODUCTION

Two-dimensional (2D) transition metal dichalcogenides (TMDCs) are characterized by strong crystal anisotropy due to weak interlayer van der Waals (vdW) interactions and strong intralayer covalent bonds, resulting in vdW layered crystal structures (*1*, *2*). Exotic physical properties, recently found in these TMDCs, are often layer-number dependent near the monolayer (ML) regime (*3*–*8*). In addition, within the unit layer, atomic-scale deformations such as point defects and grain boundaries generate distinctive 2D physical properties. For example, single point defects in WSe_2 and WS_2 MLs serve as sources for single-photon emissions (*9*, *10*) and electronic dopants (*11*, *12*), and mirror twin boundaries in $MoSe_2$ MLs provide topologically protected edge states (*13*, *14*). To translate the local physical properties into practical device platforms, these atomic-scale deformations must be deterministically embedded in the 2D host lattices of TMDC MLs over a large area, i.e., at the wafer scale (*15*, *16*). To this end, we report conformal growth of atomically thin MoS_2 and WS_2 films on wafer scale (including ML films) periodical 3D textured substrates, by controlled metal-organic chemical vapor deposition (MOCVD). Therein, the periodic 3D patterns include arrays of nanoscale needles fabricated on 4-inch quartz wafers and microscale trenches on 4-inch SiO_2/p^+-Si wafers. In addition, we demonstrate the fabrication of 3D textured membranes by delaminating deposited MoS_2 and WS_2 films from the patterned substrates.

RESULTS

Periodic arrays of sharp needles (tip radius, >10 nm) on pyramidal podia were electrochemically patterned on 4-inch quartz wafers, which then served as growth substrates, as shown in Fig. 1A (see Materials and Methods). Conformal deposition of MoS_2 ML was achieved by MOCVD using $Mo(CO)_6$ and $(C_2H_5)_2S$ precursors (Fig. 1B). Representative Raman scattering and photoluminescence (PL) spectra, collected from five different areas on the wafer (Fig. 1C) at room temperature, show the E_{2g} (386.6 cm^{-1}) and A_{1g} (406.4 cm^{-1}) vibration modes and the 1.88-eV light emission with the identical full width at half maximum of $\Delta\omega \sim 19.8$ cm^{-1} and $\Delta eV \sim 61$ meV with similar intensities. They commonly pertain to the MoS_2 ML characteristics; layer-number–dependent PL spectra are provided for comparison (fig. S1). This conformal ML is polycrystalline, with a typical grain size of ~200 to 300 nm, as shown in sequential snapshots obtained during the growth period (Fig. 1, D to F); one can identify individual triangular facets on quartz pyramids and needles in Fig. 1E, which then merge to form continuous ML films (Fig. 1F) on the quartz pyramids and needles (Fig. 1D). To verify the conformal coverage of the MoS_2 ML, transmission electron microscopy (TEM) specimens were prepared by a dry-cut method of the as-grown substrates (Fig. 1G), in which multiple arrays of MoS_2 ML on needles were characterized one by one by focusing individual needles located on different focal planes (e.g., in Fig. 1H, the outlined needle is in focus, but the rests are out of focus). The high-resolution TEM (HRTEM) image in Fig. 1I exhibits the conformal ML coverage over the entire needle surfaces. High-angle annular dark-field (HAADF) scanning TEM (STEM) image reveals the conformal atomic structure of the MoS_2 ML on the edge of a needle (see the magnified image and atomic model in Fig. 1J). The chemical composition of the MoS_2 ML was identified via energy dispersive x-ray spectroscopy (EDS) elemental mapping in the STEM operated at 60 kV (Fig. 1K).

We have also demonstrated the conformal deposition of MoS_2 ML on SiO_2/p^+-Si trench substrates, which were periodically patterned with various pitch distances at the micrometer scale (Fig. 2, A and B); the square patterns of different colors shown in the optical microscopy (OM) image in Fig. 2A are due to the different pitch distances (fig. S2). The cross-sectional HAADF-STEM images directly confirm the conformal deposition of MoS_2 ML on these trenches (Fig. 2C). Similar to the growth on quartz pyramids and needles, polycrystalline texturing was achieved; discrete ML crystal facets (~200 to 300 nm in size) were conformally grown on the trenches (Fig. 2D) to form continuous ML films (Fig. 2, E and F). PL mapping images (Fig. 2G), focused on either the top or bottom of the trenches, show a uniform

[1]Center for Artificial Low Dimensional Electronic Systems, Institute for Basic Science (IBS), Pohang 37673, Republic of Korea. [2]Department of Materials Science and Engineering, Pohang University of Science and Technology (POSTECH), Pohang 37673, Republic of Korea. [3]Department of Chemistry and Chemical Biology and Department of Physics, Harvard University, Cambridge, MA 02138, USA. [4]Department of Energy Science, Sungkyunkwan University, Suwon 16419, Republic of Korea.
*These authors contributed equally to this work.
†Corresponding author. Email: mhjo@postech.ac.kr

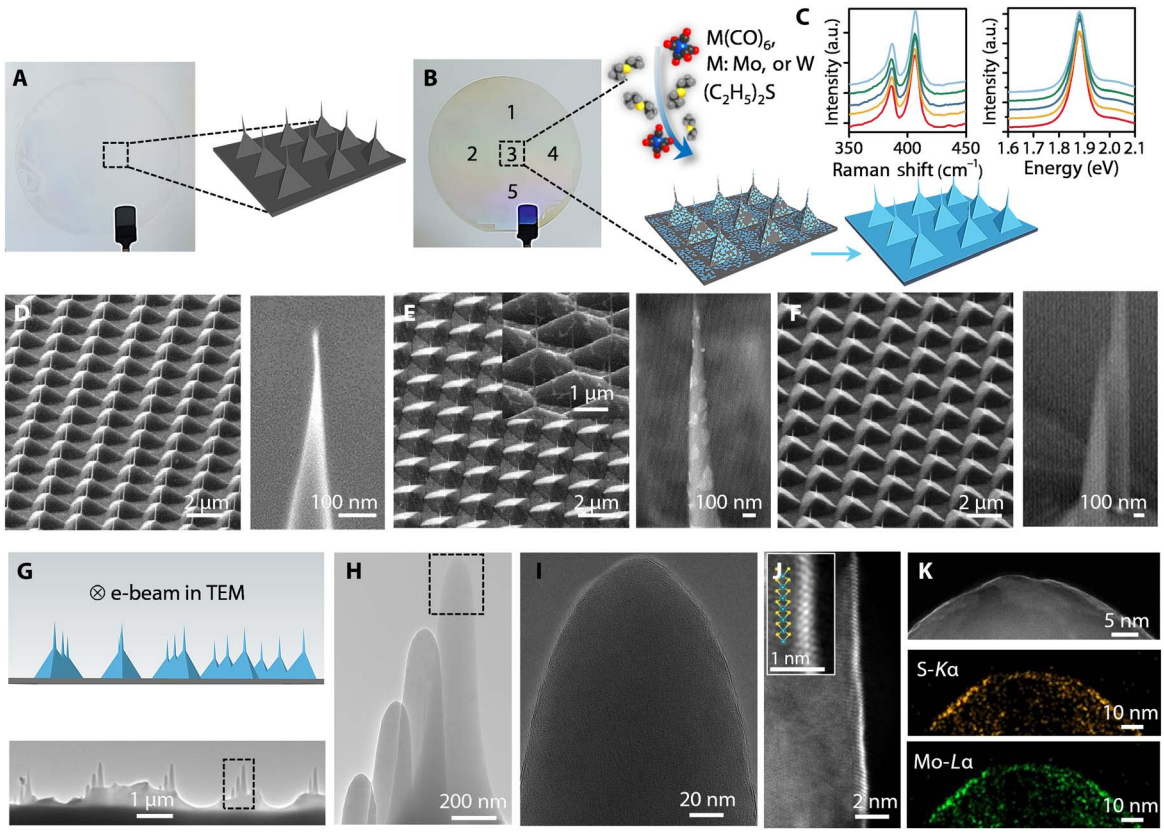

Fig. 1. Conformal deposition of 3D TMDC ML films on a quartz needle array. (**A** and **B**) Schematic of the growth of TMDC ML films on a 4-inch wafer-scale quartz needle array, with photographs of (A) pristine and (B) as-grown MoS_2 on a quartz wafer. (**C**) Raman and PL spectra measured from marked spots of as-grown MoS_2 ML on a quartz wafer. (**D** to **F**) scanning electron microscopy (SEM) images of (D) pristine arrays of pyramids and needles and (E) partially and (F) fully covered MoS_2 ML film on pyramids and needles. Inset: A partially covered MoS_2 ML on the pyramidal podia. (**G**) Low-magnification and (**H**) high-magnification TEM images of multiple arrays of needles covered with a MoS_2 ML. (**I**) HRTEM image of a conformal MoS_2 ML on a needle. (**J**) HAADF-STEM image at the side region. Inset: Magnified HAADF-STEM image with an atomic model of the MoS_2 ML. (**K**) HAADF-STEM image at the tip region with corresponding STEM-EDS elemental maps obtained by characteristic S-K_α and Mo-L_α x-ray signals. a.u., arbitrary units; e-beam, electron beam.

PL intensity distribution for the MoS_2 ML, suggesting uniform and conformal ML coverage over the 3D trenches. To verify a reliable ML channel connection along with the trench coverage, we patterned Au electrodes over various channel lengths by electron beam (e-beam) lithography/lift-off and fabricated field-effect transistor (FET) devices (Fig. 2H and fig. S3) across multiple trenches. Using the transfer length method, we confirmed that continuous and uniform channels were formed over multiple trenches, where the channel resistance was found to be linearly proportional to the length; see also fig. S4 for results at the millimeter length scale. By direct comparison with FETs formed on flat ML without trenches, we have also extracted the sheet resistance (R_s) to be 6.45 megohm, which is slightly higher than 4.88 megohm at the flat ML regions; see also fig. S5. Accordingly, we measured the contact resistance (R_c) as 324 kilohm μm, which is also slightly higher than 226 kilohm μm at the flat ML regions (Fig. 2I). The higher channel resistance can be attributed to complex grain boundaries over the trench edges, as further discussed below. The transfer curves (V_g-dependent I_d at V_d = 0.1 V) show the similar n-type channel characteristics with a lower FET mobility of 3.0 $cm^2\ V^{-1}\ s^{-1}$ compared with 4.5 $cm^2\ V^{-1}\ s^{-1}$ for flat ML regions (Fig. 2J).

Using $W(CO)_6$ and $(C_2H_5)_2S$ precursors, we have also achieved the conformal growth of WS_2 MLs on an array of sharp SiO_2/p^+-Si needles patterned on a 4-inch wafer. The ML uniformity of WS_2 regarding its semiconductor properties was verified via PL mapping across the ML tip (1 μm in height) arrays, as shown in the OM image in Fig. 3A. The PL intensity was regularly enhanced at the needles, and the periodicity matched the needle pitch (Fig. 3B); see fig. S6 for a comparison with results from ML TMDC films on planar substrates. At the ML tips, the PL intensity is enhanced by about five times compared with that at the flat region (Fig. 3, C and D) because of the geometrically enhanced optical field at the needle curvature; see Fig. 3E and fig. S7 for similar Raman intensity variations. In any case, both the characteristic PL and Raman peaks remain spectroscopically identical regardless of the position within the 3D ML film, with the consistent peak energies (1.99 eV and 353 cm^{-1}) and the full width at half maximum (65 to 68 meV and 13.4 cm^{-1}), confirming the ML uniformity; see fig. S8 for similar growth characteristics of 3D MoS_2 films and fig. S9 for the second harmonic generation experiments. These conformally continuous 3D WS_2 films can be easily delaminated from the growth substrates to form suspended membranes, allowing them to float in deionized (DI) water, because of the weak vdW interaction with the quartz substrates (Fig. 3F); see fig. S10 and movie S1 for the delamination process. It turned out that the ML membranes inevitably collapsed at the needle regions during drying of the DI water on the TEM grids presumably because of a finite capillary force at the sharp needle curvature (fig. S11). Nevertheless, it is

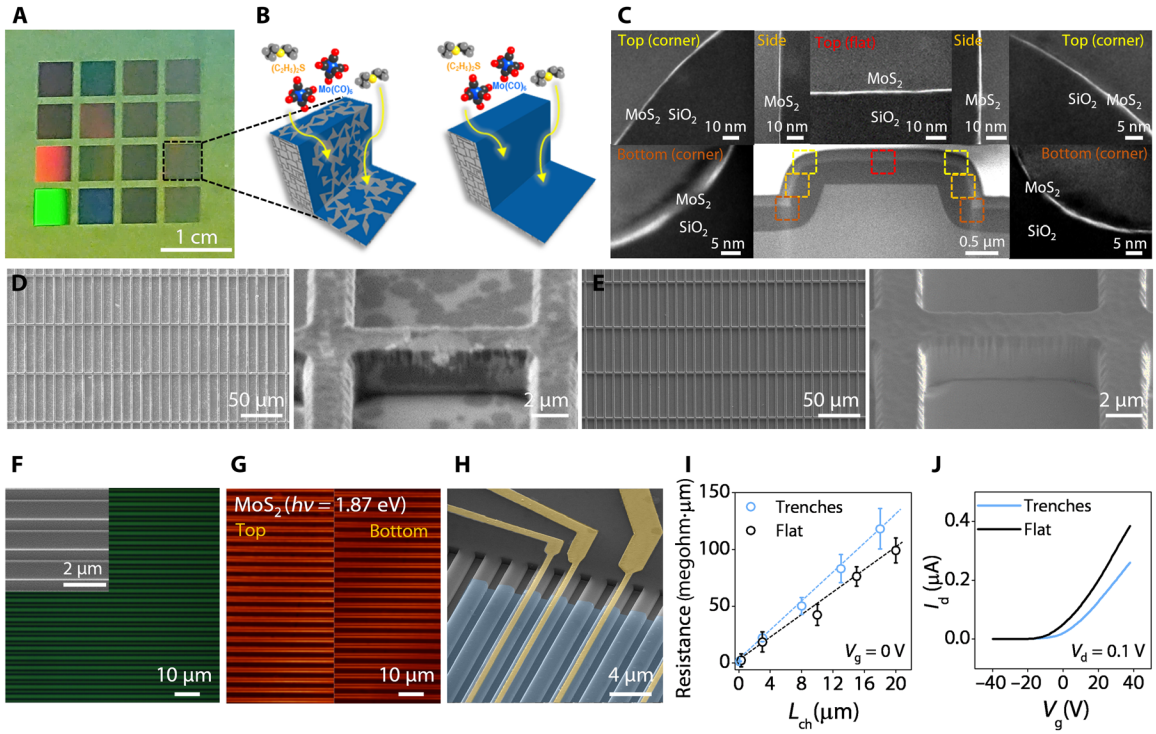

Fig. 2. Growth of 3D TMDCs on microscale trenches with reliable formation of semiconducting channels. (**A**) Photograph of wafer-scale SiO_2/p^+-Si trench-patterned substrate. (**B**) Schematic for conformal growth of MoS_2 ML film using MOCVD. (**C**) Cross-sectional HAADF-STEM images of a MoS_2 ML on microscale SiO_2 trench. (**D** to **E**) SEM images of (D) partially and (E) fully covered MoS_2 ML films on SiO_2 trenches. (**F**) OM image of conformally deposited MoS_2 ML on trenches. Inset: Magnified SEM image of the substrate. (**G**) PL images focused on the top (left) and bottom surface (right) at MoS_2 A exciton peak ($h\nu$ = 1.88 eV). (**H**) False-color SEM image of FET devices for transfer length method along 3D MoS_2 ML channels (light blue, MoS_2; yellow, metal contact). (**I**) L_{ch}-dependent resistance at V_g = 0 V. (**J**) Transfer (I-V_g) curves at V_d = 0.1 V along 3D MoS_2 ML channels on the trench (light blue) and flat region (black).

remarkable to observe that the few-layer films robustly survived, as shown by in-plane TEM images, where the pyramidal and needle shapes were intact in the delaminated membranes (Fig. 3G); see also movie S2. We observed different selected-area electron diffraction (SAED) patterns (Fig. 3H) from the planar (yellow) and pyramidal (red) regions, which can be attributed to different diffraction paths of e-beams, associated with the different crystal angles with respect to the base plane of the substrate (Fig. 3I); see fig. S12 for detailed analyses of the electron diffraction pattern observed on the needles. We acquired PL spectra for the MoS_2 and WS_2 films, including ML films, before and after delamination and observed nearly identical spectral features, except for the slight blue shift of 20 to 30 meV (fig. S13). The Raman spectra were also identical. These observations suggest that the suspended membranes preserve their original crystal textures upon delamination. Clearly, these atomically thin membranes are conformally continuous at the sharp needle tips, as well as in the side (flatter) regions (Fig. 3, J to M). We found that the polycrystalline textures are maintained with the characteristic grain boundaries, particularly at the tip curvature (radius of ~30 nm). We confirmed that identically thick WS_2 layers (7.8 nm; 13 layers) were conformally deposited on the needles, regardless of the aspect ratio, to form continuous 3D films.

DISCUSSIONS

The vdW ML epitaxy is characterized by a weak interaction of the deposited MLs with the target substrate; thus, in principle, ML crystal growth on a flat 2D substrate is not strictly affected by local variations on the substrates, such as morphologies, crystal texture, and strain (*17*). Our 3D ML growth proceeded in the near-equilibrium regime (*18*). As we observed stable crystal facets shown in Fig. 4A, the growth is dictated by surface energy minimization during crystallization, followed by subsequent edge growth to form continuous ML films (*19*, *20*). Then, to kinetically accommodate this ML crystallization over periodic 3D textures at the nanometer scale, i.e., lateral 3D textured ML crystallization, we maintained a slow lateral growth rate of 0.15 nm/min by controlling the flow rate of MO sources with low partial pressures ($p_{Mo(CO)6} \sim 10^{-5}$ torr) during MOCVD for MoS_2 and WS_2 ML (Fig. 4, B to D); see the Supplementary Materials for a growth rate estimation. Conventional powder CVD growth (Fig. 4E) (*21*), in which substantially higher precursor vapor pressure ($p_{MoO3} \sim 10^{-2}$ torr) is usually generated from solid precursors, produces a much higher growth rate (*22*), i.e., ~1500 nm/min in our case, and resulted in nonuniform coverage on periodic 3D textures (Fig. 4, F to H, and fig. S14). The primary process variables defining the conformal growth characteristics include the partial pressure of precursors and the resultant growth rates, determining the sticking coefficient, β, as a key parameter (*23*, *24*). In thin film deposition, conformality depends on the reactive sticking probability of adatoms, where β is defined as the ratio of the number of adsorbate atoms (flux sticking) to atoms that impinge upon the surface (incident flux). Thus, the lower β values enable deeper diffusion of the adatoms into the 3D features, leading to better conformality. Specifically, β can be expressed as $\beta = \frac{\text{flux sticking}}{\text{incident flux}} = \frac{\nu/\rho}{p/\sqrt{2\pi mkT}}$, where ν is the lateral growth rate (nm/min),

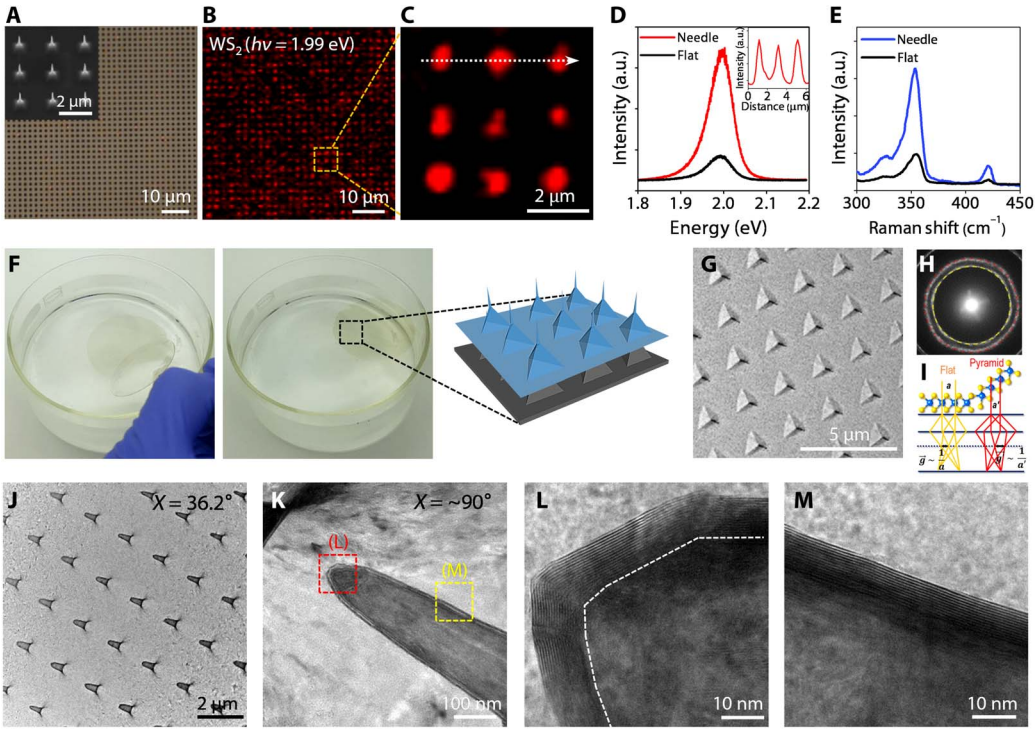

Fig. 3. Optical properties of 3D TMDC ML films on a needle array and their membranes by delamination from 3D textured substrates. (**A**) OM image of a conformally coated WS_2 ML on a SiO_2/p^+-Si needle array. Inset: Magnified SEM image of the substrate. (**B**) Large-area PL image at the WS_2 exciton peak ($h\nu$ = 1.99 eV) obtained from the region corresponding to (A). (**C**) Magnified PL image. (**D**) PL and (**E**) Raman spectra obtained from the needle region (red and blue) and flat region (black). Inset: PL intensity line profile indicated in (C). (**F**) Photographs of the peel-off process and illustration of a delaminated vdW WS_2 membrane separated from the 3D substrate. Photo credit: Gangtae Jin, Pohang University of Science and Technology. (**G**) Low-magnification TEM image of a few-layer 3D WS_2 membrane at a −36.2° tilt angle. (**H**) SAED pattern of the 3D WS_2 membrane. (**I**) Diffracted beam path for planar and tilted TMDC crystals on the pyramidal array. (**J**) Low-magnification TEM image of the suspended WS_2 needle array at the 36.2° tilt angle. (**K**) Low-magnification TEM image of sharp 13-L WS_2 needle at a tilt angle of approximately 90°. (**L** and **M**) High-magnification TEM images of the (L) tip region (red) and (M) side region (yellow) of the WS_2 needle.

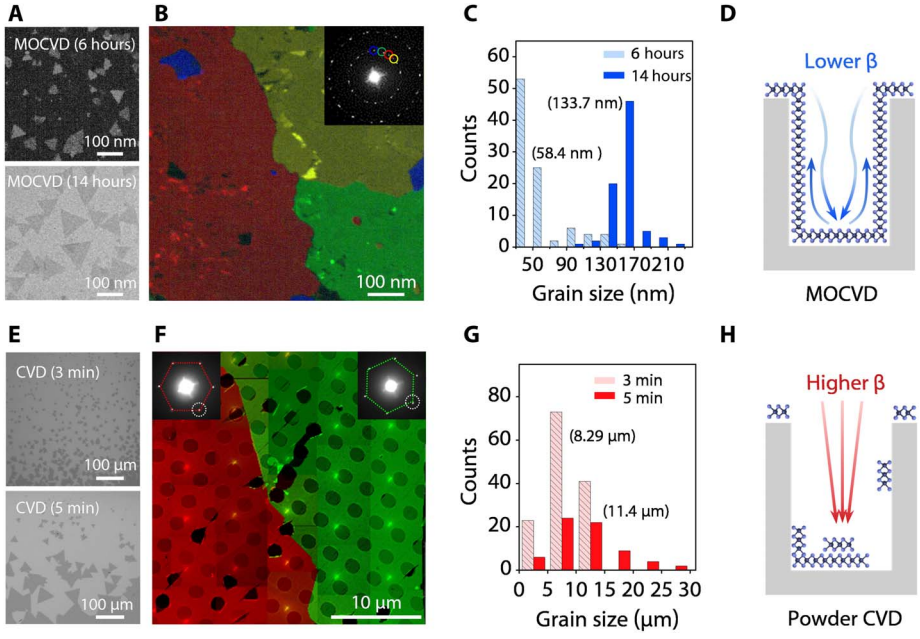

Fig. 4. Kinetic origin of conformal ML deposition via MOCVD process. (**A**) TEM images of MOCVD-grown MoS_2 crystals for different growth time. (**B**) False-color dark-field (DF) TEM image of suspended MOCVD-grown MoS_2 ML film on holey carbon grid. (**C**) Grain size distribution of MOCVD MoS_2 crystals. (**D**) Schematic of 3D ML texturing by MOCVD. (**E**) OM images of powder CVD-grown MoS_2 crystals for different growth time. (**F**) DF-TEM image of powder CVD-grown MoS_2 MLs. Inset: SAED pattern from MoS_2 ML film. (**G**) Grain size distribution of powder CVD-grown MoS_2. (**H**) Schematic of CVD-grown MLs from solid powder precursors.

p is the partial pressure of precursors, ρ is the areal density of the adatoms, m is the mass of the precursor molecules, k is Boltzmann's constant, and T is the growth temperature (*25*). In our study, setting the T and p to be 535°C and 4.2×10^{-5} torr and 680°C and 1.0×10^{-2} torr for MOCVD and powder CVD, we found the ratio, $\beta_{MOCVD}/\beta_{PowderCVD}$, to be ~35, using a ν_{MOCVD} of 0.15 nm/min and a $\nu_{PowderCVD}$ of 1500 nm/min. To further investigate this critical role of β for ML conformality, we conducted MOCVD growth at a higher p of 7.8×10^{-4} torr, resulting in a higher growth rate of ~1.3 nm/min (*26*). In this case, we observed poor conformality at the top and bottom trench surfaces, as shown in fig. S15. Thereby, we conclude that a key factor for achieving conformal 3D texturing in the vdW ML epitaxy is the slow kinetic control of the 2D edge growth.

MATERIALS AND METHODS

Quartz nanoneedle array fabrication

Single-crystal z-cut quartz wafers (MTI Corporation, USA) were pretreated via sonication with acetone and isopropyl alcohol, followed by oxygen plasma treatments; then, a 60-nm-thick Cr layer was evaporated (Denton Vacuum, USA) on top of the quartz substrates. For short nanoneedles, e-beam lithography (ELS-F125, Elionix, USA) was used to produce a square array of circular features using FOx-16 negative e-beam resist (Dow Corning, USA), with diameters ranging from 100 to 200 nm. The FOx-16 was diluted with methyl isobutyl ketone (1:2 by volume) to achieve ~100-nm thickness after spin-coating and was soft-baked at 80°C for 4 min. The e-beam writing dosage was 3000 μC/cm^2, and the samples were developed in a 25% aqueous solution of tetramethylammonium hydroxide (Sigma-Aldrich, USA). For a wafer-scale nanoneedle array, photolithography (AutoStep 200, GCA, USA) was used to pattern the photoresist (MEGAPOSIT SPR 955, Dow, USA) with a circular diameter of 1 μm across an entire 4-inch wafer after development in MF CD-26 developer (MicroChem, USA). The resist patterns were transferred to metal feature arrays via reactive ion etching (PlasmaPro 100 Cobra 300, Oxford Instruments, UK) to selectively remove Cr layers. The Cr features were used as a hard mask for subsequent SiO_2 wet-etching, performed by soaking the patterned substrate in a 1:5 mixture solution of 49% hydrofluoric acid (HF) and 40% ammonium fluoride (NH_4F). The etching temperature was varied from 25° to 55°C. During the wet-etching process, the quartz substrates were removed from the etching solution to allow for inspection of the etching process until approximately 50% of the metal hard masks had fallen off the needles. Then, the substrates were rinsed in Cr etchant 1020 (Transene Inc., USA) to remove the remaining metal and were cleaned with piranha solution to remove contaminants. The pillar height and wet-etching duration are linearly dependent on the diameter of the Cr hard masks and are also closely related to the etching conditions. To fabricate pillars with a height of 2 μm, 200-nm-diameter hard masks were used, and the etching time in a 1:5 mixture of HF and NH_4F at 25°C was ~200 min. To etch a 1-μm Cr mask in 1:5 etchant at 55°C, the typical etching time was ~150 min.

Fabrication of SiO_2 needles on a Si wafers

A layer of photoresist (MEGAPOSIT SPR 955, Dow, USA) was spin-coated on top of a 4-inch Si (100) wafer (NOVA Electronic Materials, USA) at 4000 rpm and baked at 90°C for 90 s. Then, an i-line stepper (AutoStep 200, GCA, USA) was used to pattern a square array of circular features across the entire wafer. The resist was baked again at 115°C for 90 s and developed in MF CD-26 developer (MicroChem, USA) for 60 s to generate 1-μm resist features. The resist pattern was used as an etching mask for Si etching in a deep reactive ion etcher (Omega LPX Rapier, SPTS, UK) to generate 2-μm-tall Si pillars. Later, the etched Si wafer was cleaned, following the standard Radio Corporation of America (RCA) cleaning protocols. The Si pillars were dry-oxidized in a tube furnace (Tystar, USA) at 1150°C for 8 hours, and the resulting grown oxide was removed in a 5:1 buffered oxide etchant (MicroChemicals, USA), resulting in periodic Si nanoneedles with a tip diameter of less than 100 nm. Additional steps of thermal oxidization at 950°C and etching were performed if the needle diameter was larger than 100 nm. The Si wafer was oxidized again at 1150°C for 2 hours to transform the Si nanoneedles to SiO_2 nanoneedles with tip diameters of approximately 200 nm.

Growth of 4-inch wafer-scale ML MoS_2 by MOCVD

The growth of 4-inch wafer-scale MoS_2 MLs was achieved using high-purity gas precursors, $Mo(CO)_6$ (99.9%; Sigma-Aldrich) and $(C_2H_5)_2S$ (98%; Sigma-Aldrich). Four-inch quartz and SiO_2/p^+-Si wafers were placed in the center of a 6-inch hot-walled quartz tube furnace. Before the MOCVD process, the furnace was purged for 1 hour to eliminate residual contaminants, and the temperature was ramped up to 535°C for 30 min. The growth proceeded for 26 hours with partial pressure of precursors of 4.2×10^{-5} torr for $Mo(CO)_6$ and 10^{-2} torr for $(C_2H_5)_2S$. The base pressure of the reactor was ~7 torr under the carrier gas flow of 150 standard cubic centimeters per minute (sccm) for Ar (99.9999%) and 1 sccm for H_2 (99.9999%).

Water-assisted transfer of 3D TMDC membranes

Delamination and transfer of TMDC membranes can be conducted without the typical spin-coating process of polymer layers (polymethyl methacrylate and polystyrene) and removers (acetone and toluene). The outer edges of pristine TMDC films grown on 3D textured substrates were gently carved with a knife. The newly exposed SiO_2 surface was dipped into DI water, and the water penetrated the interface between the TMDCs and SiO_2 because of their difference in wettability. The entire 3D TMDC membrane, floating on water, was picked up onto an arbitrary substrate. Last, the transferred 3D TMDC membranes were naturally dried under ambient conditions.

SUPPLEMENTARY MATERIALS

Supplementary material for this article is available at http://advances.sciencemag.org/cgi/content/full/5/7/eaaw3180/DC1

Fig. S1. Layer-number–dependent PL spectra (ML and bilayer) of MoS_2 and WS_2 films.
Fig. S2. OM images as different pitch sizes in patterned SiO_2/p^+-Si trenches.
Fig. S3. False-color SEM image of the FET devices on flat regions.
Fig. S4. Length-dependent resistance of 3D MoS_2 ML films on microtrench substrates up to l mm.
Fig. S5. Length-dependent FET characteristics of 3D MoS_2 ML films on microtrench substrates.
Fig. S6. PL intensity maps and the corresponding PL spectra of TMDC ML films on planar SiO_2/p^+-Si substrates.
Fig. S7. Raman mapping of 3D WS_2 ML films on SiO_2/p^+-Si needle arrays.
Fig. S8. Raman and PL mapping of 3D MoS_2 ML films on SiO_2/p^+-Si needle arrays.
Fig. S9. Second harmonic generation in MoS_2.
Fig. S10. Schematic illustration of the DI water–assisted transfer of 3D TMDC membranes.
Fig. S11. TEM images of delaminated WS_2 ML films on a TEM grid.
Fig. S12. Local diffraction patterns generated on the 3D WS_2 membranes.
Fig. S13. PL and Raman spectra of MoS_2 ML and WS_2 ML films before and after delamination.
Fig. S14. Nonconformal MoS_2 film growth on microtrench substrates by a powder CVD method.
Fig. S15. MOCVD growth of MoS_2 films on 3D trench substrates at a faster growth rate.
Section S1. Pyramid structure analysis using the diffraction patterns
Section S2. Determination of sticking coefficients
Section S3. Powder CVD growth of MoS_2 ML crystals

Movie S1. Peeling off the WS_2 ML films from the quartz substrates by immersing in DI water.
Movie S2. TEM tilting of suspended 3D WS_2 membranes.

REFERENCES AND NOTES

1. A. K. Geim, I. V. Grigorieva, Van der Waals heterostructures. *Nature* **499**, 419–425 (2013).
2. Y. Liu, N. O. Weiss, X. Duan, H.-C. Cheng, Y. Huang, X. Duan, Van der Waals heterostructures and devices. *Nat. Rev. Mater.* **1**, 16042 (2016).
3. A. Splendiani, L. Sun, Y. Zhang, T. Li, J. Kim, C.-Y. Chim, G. Galli, F. Wang, Emerging photoluminescence in monolayer MoS_2. *Nano Lett.* **10**, 1271–1275 (2010).
4. D. Xiao, G.-B. Liu, W. Feng, X. Xu, W. Yao, Coupled spin and valley physics in monolayers of MoS_2 and other group-VI dichalcogenides. *Phys. Rev. Lett.* **108**, 196802 (2012).
5. X. Xi, L. Zhao, Z. Wang, H. Berger, L. Forró, J. Shan, K. F. Mak, Strongly enhanced charge-density-wave order in monolayer $NbSe_2$. *Nat. Nanotechnol.* **10**, 765–769 (2015).
6. M.-J. Lee, J.-H. Ahn, J. H. Sung, H. Heo, S. G. Jeon, W. Lee, J. Y. Song, K.-H. Hong, B. Choi, S.-H. Lee, M.-H. Jo, Thermoelectric materials by using two-dimensional materials with negative correlation between electrical and thermal conductivity. *Nat. Commun.* **7**, 12011 (2016).
7. H. Heo, J. H. Sung, S. Cha, B.-G. Jang, J.-Y. Kim, G. Jin, D. Lee, J.-H. Ahn, M.-J. Lee, J. H. Shim, H. Choi, M.-H. Jo, Interlayer orientation-dependent light absorption and emission in monolayer semiconductor stacks. *Nat. Commun.* **6**, 7372 (2015).
8. B. Huang, G. Clark, E. Navarro-Moratalla, D. R. Klein, R. Cheng, K. L. Seyler, D. Zhong, E. Schmidgall, M. A. McGuire, D. H. Cobden, W. Yao, D. Xiao, P. Jarillo-Herrero, X. Xu, Layer-dependent ferromagnetism in a van der Waals crystal down to the monolayer limit. *Nature* **546**, 270–273 (2017).
9. Y.-M. He, G. Clark, J. R. Schaibley, Y. He, M.-C. Chen, Y.-J. Wei, X. Ding, Q. Zhang, W. Yao, X. Xu, C.-Y. Lu, J.-W. Pan, Single quantum emitters in monolayer semiconductors. *Nat. Nanotechnol.* **10**, 497–502 (2015).
10. A. Srivastava, M. Sidler, A. V. Allain, D. S. Lembke, A. Kis, A. Imamoğlu, Optically active quantum dots in monolayer WSe_2. *Nat. Nanotechnol.* **10**, 491–496 (2015).
11. S.-Y. Seo, J. Park, J. Park, K. Song, S. Cha, S. Sim, S.-Y. Choi, H. W. Yeom, H. Choi, M.-H. Jo, Writing monolithic integrated circuits on a two-dimensional semiconductor with a scanning light probe. *Nat. Electron.* **1**, 512–517 (2018).
12. S. McDonnell, R. Addou, C. Buie, R. M. Wallace, C. L. Hinkle, Defect-dominated doping and contact resistance in MoS_2. *ACS Nano* **8**, 2880–2888 (2014).
13. S. Barja, S. Wickenburg, Z.-F. Liu, Y. Zhang, H. Ryu, M. M. Ugeda, Z. Hussain, Z.-X. Shen, S.-K. Mo, E. Wong, M. B. Salmeron, F. Wang, M. F. Crommie, D. F. Ogletree, J. B. Neaton, A. Weber-Bargioni, Charge density wave order in 1D mirror twin boundaries of single-layer $MoSe_2$. *Nat. Phys.* **12**, 751–756 (2016).
14. H. Liu, L. Jiao, F. Yang, Y. Cai, X. Wu, W. Ho, C. Gao, J. Jia, N. Wang, H. Fan, W. Yao, M. Xie, Dense network of one-dimensional midgap metallic modes in monolayer $MoSe_2$ and their spatial undulations. *Phys. Rev. Lett.* **113**, 066105 (2014).
15. K. Kang, S. Xie, L. Huang, Y. Han, P. Y. Huang, K. F. Mak, C.-J. Kim, D. Muller, J. Park, High-mobility three-atom-thick semiconducting films with wafer-scale homogeneity. *Nature* **520**, 656–660 (2015).
16. A. M. van der Zande, P. Y. Huang, D. A. Chenet, T. C. Berkelbach, Y. You, G.-H. Lee, T. F. Heinz, D. R. Reichman, D. A. Muller, J. C. Hone, Grains and grain boundaries in highly crystalline monolayer molybdenum disulphide. *Nat. Mater.* **12**, 554–561 (2013).
17. A. Koma, Van der Waals epitaxy—A new epitaxial growth method for a highly lattice-mismatched system. *Thin Solid Films* **216**, 72–76 (1992).
18. Z. Zhang, M. G. Lagally, Atomistic processes in the early stages of thin-film growth. *Science* **276**, 377–383 (1997).
19. T. Ma, W. Ren, X. Zhang, Z. Liu, Y. Gao, L.-C. Yin, X.-L. Ma, F. Ding, H.-M. Cheng, Edge-controlled growth and kinetics of single-crystal graphene domains by chemical vapor deposition. *Proc. Natl. Acad. Sci. U.S.A.* **110**, 20386–20391 (2013).
20. D. Cao, T. Shen, P. Liang, X. Chen, H. Shu, Role of chemical potential in flake shape and edge properties of monolayer MoS_2. *J. Phys. Chem. C* **119**, 4294–4301 (2015).
21. H. Heo, J. H. Sung, G. Jin, J.-H. Ahn, K. Kim, M.-J. Lee, S. Cha, H. Choi, M.-H. Jo, Rotation-misfit-free heteroepitaxial stacking and stitching growth of hexagonal transition-metal dichalcogenide monolayers by nucleation kinetics controls. *Adv. Mater.* **27**, 3803–3810 (2015).
22. W. Chen, J. Zhao, J. Zhang, L. Gu, Z. Yang, X. Li, H. Yu, X. Zhu, R. Yang, D. Shi, X. Lin, J. Guo, X. Bai, G. Zhang, Oxygen-assisted chemical vapor deposition growth of large single-crystal and high-quality monolayer MoS_2. *J. Am. Chem. Soc.* **137**, 15632–15635 (2015).
23. J. J. Hsieh, Influence of surface-activated reaction kinetics on low-pressure chemical vapor deposition conformality over micro features. *J. Vac. Sci. Technol. A.* **11**, 78–86 (1993).
24. S. M. Gates, Surface chemistry in the chemical vapor deposition of electronic materials. *Chem. Rev.* **96**, 1519–1532 (1996).
25. N. Kumar, A. Yanguas-Gil, S. R. Daly, G. S. Girolami, J. R. Albelson, Growth inhibition to enhance conformal coverage in thin film chemical vapor deposition. *J. Am. Chem. Soc.* **130**, 17660–17661 (2008).
26. D. M. Andoshe, G. Jin, C.-S. Lee, C. Kim, K. C. Kwon, S. Choi, W. Sohn, C. W. Moon, S. H. Lee, J. M. Suh, S. Kang, J. Park, H. Heo, J. K. Kim, S. Han, M.-H. Jo, H. W. Jang, Directly assembled 3D molybdenum disulfide on silicon wafer for efficient photoelectrochemical water reduction. *Adv. Sustain. Syst.* **2**, 1700142 (2018).

Acknowledgments
Funding: This work was supported by the Institute for Basic Science (IBS), Korea under project code IBS-R014-A1 (to M.-H.J.) and the Vannevar Bush Faculty Fellowship (N00014-16-1-2825 to H.P.). **Author contributions:** M.-H.J., G.J., C.-S.L., H.P., and X.L. conceived and designed the project. G.J., C.-S.L., and H.H. conducted MOCVD growth experiments and material characterizations. X.L. fabricated the 3D wafers. Juho Kim performed electrical characterizations. C.H. and Jonghwan Kim carried out the optical measurements. Z.W., O.F.N.O., B.P., and J.P. performed the TEM measurements. S.H.O. and S.-Y.C. analyzed the data. M.-H.J., X.L., and H.P. cowrote the paper. All the authors discussed the results and commented on the manuscript. **Competing interests:** The authors declare that they have no competing interests. **Data and materials availability:** All data needed to evaluate the conclusions in the paper are present in the paper and/or the Supplementary Materials. Additional data related to this paper may be requested from the authors.

Submitted 8 December 2018
Accepted 17 June 2019
Published 26 July 2019
10.1126/sciadv.aaw3180

Citation: G. Jin, C.-S. Lee, X. Liao, J. Kim, Z. Wang, O. F. N. Okello, B. Park, J. Park, C. Han, H. Heo, J. Kim, S. H. Oh, S.-Y. Choi, H. Park, M.-H. Jo, Atomically thin three-dimensional membranes of van der Waals semiconductors by wafer-scale growth. *Sci. Adv.* **5**, eaaw3180 (2019).